

**Czech Technical University in  
Prague**

**Faculty of Nuclear Sciences and Physical  
Engineering**

Department of Physics



**Quarkonia studies using the  
ATLAS detector at the  
LHC**

Research Project

**Bc. Radek Novotný**

Supervisor: Ing. Michal Marčíšovský  
Prague, 2015



České vysoké učení technické v  
Praze  
Fakulta jaderná a fyzikálně inženýrská

Katedra Fyziky



Studium kvarkonií na  
urychlovači LHC pomocí  
detektoru ATLAS

Výzkumný úkol

**Bc. Radek Novotný**  
Vedoucí práce: Ing. Michal Marčíšovský  
Praha, 2015



*Title:* **Quarkonia studies using the ATLAS detector at the LHC**

*Author:* Bc. Radek Novotný

*Field of study:* Nuclear Engineering

*Specialization:* Experimental Nuclear and Particle Physics

*Sort of project:* Research project

*Supervisor:* Ing. Michal Marčišovský

---

*Abstract:*

The quarkonium is bound state of a heavy quark and antiquark of the same flavour. It is the simplest system bound by a combination of strong and electromagnetic interactions. Since the binding energies of the quarkonia systems are at the edge of perturbative QCD energy scale, study of the  $Q\bar{Q}$  system properties serves to improve the understanding of the strong force. The most widely known state of charmonium is the  $J/\psi$  resonance, which can decay via electromagnetic interaction into a  $\mu^+\mu^-$  or  $e^+e^-$  pair, easily observed in detector. The first excited state of the  $J/\psi$  resonance is called  $\psi(2S)$  and as well as  $J/\psi$  can decay into a  $\mu^+\mu^-$  or  $e^+e^-$  pair.

This research project is devoted to the measurement of the double-differential inclusive  $J/\psi \rightarrow \mu^+\mu^-$  and  $\psi(2S) \rightarrow \mu^+\mu^-$  production cross section in proton-proton collisions measured by the ATLAS detector at the Large Hadron Collider (LHC). Furthermore, the measurement of fraction of  $J/\psi$  and  $\psi(2S)$  produced indirectly from the decay of  $B$  mesons is presented.

In the beginning of this research project, the Standard Model of particles and interactions, the ATLAS experiment and the elementary properties of the quarkonia are briefly introduced. In the following chapters, the analysis procedure and results are presented.

*Key words:*  $J/\psi$ , quarkonia, ATLAS, LHC, Standard Model, non-prompt production

**Název práce: Studium kvarkonií na urychlovači LHC pomocí detektoru ATLAS**

*Autor:* Bc. Radek Novotný

*Obor studia:* Jaderné inženýrství

*Zaměření:* Experimentální Jaderná a Částicová Fyzika

*Druh práce:* Výzkumný úkol

*Vedoucí práce:* Ing. Michal Marčišovský

---

*Abstrakt:*

Kvaronium je vázaná stav těžkého kvarku a příslušného antikvarku stejné vůně. Jakožto nejjednodušší systémem svázaný silnou interakcí, slouží ke studiu vlastností této síly. Jedním ze zástupců kvarkonií je charmonium skládající se z charm kvarku a antikvarku. Základním stavem charmonia je dobře známá rezonance  $J/\psi$ , která se může rozpadat pomocí slabé interakce například na  $\mu^+\mu^-$  nebo  $e^+e^-$ . Prvním excitovaným stavem  $J/\psi$  je částice nazvaná  $\psi(2S)$ , která se také může rozpadat na  $\mu^+\mu^-$  nebo  $e^+e^-$ .

Tato práce se zabývá se měřením diferenciálního účinného průřezu při inkluzivní produkci jak  $J/\psi \rightarrow \mu^+\mu^-$  tak  $\psi(2S) \rightarrow \mu^+\mu^-$  určené na citlivé oblasti detektoru ATLAS. Detektor ATLAS se nachází na velkém hadronovém urychlovači LHC v laboratoři CERN a pro účel této práce byly použity pouze data z proton-protonových srážek. Tato práce se dále zabývá měřením podílu  $J/\psi$  a  $\psi(2S)$  vyprodukovaných z rozpadu  $B$  mezonů.

Úvodní část této práce se věnuje základnímu popisu Standardního modelu a experimentu ATLAS. Dále jsou uvedeny stručné informace o kvarkoniích a modelech jakými se popisují. V poslední části je popsán proces, jakým jsou data zpracována. Závěrem této práce jsou prezentovány výsledky měření.

*Klíčová slova:*  $J/\psi$ , kvarkonia, ATLAS, LHC, Standardní Model, nepřímá produkce

# Contents

<b>1</b>	<b>Introduction</b>	<b>1</b>
<b>2</b>	<b>Theoretical background</b>	<b>2</b>
2.1	Standard model . . . . .	2
2.1.1	Fundamental interactions . . . . .	2
2.1.2	Quarks . . . . .	3
2.1.3	Leptons . . . . .	3
2.1.4	Antiparticles . . . . .	4
2.2	Strong interaction . . . . .	4
2.2.1	Colour . . . . .	4
2.2.2	QCD . . . . .	5
2.2.3	Running coupling . . . . .	6
2.3	Heavy quarkonia production . . . . .	7
2.3.1	Color Singlet Model . . . . .	8
2.3.2	Color Evaporation Model . . . . .	8
2.3.3	Nonrelativistic QCD Factorization Model . . . . .	8
2.4	$k_t$ -factorization approach [1] . . . . .	9
<b>3</b>	<b>The ATLAS detector [2]</b>	<b>10</b>
3.1	Inner detector . . . . .	11
3.1.1	Pixel detector . . . . .	11
3.1.2	SCT detector . . . . .	12
3.1.3	Transition radiation tracker . . . . .	12
3.2	Calorimetry . . . . .	12
3.3	Muon spectrometer . . . . .	13
<b>4</b>	<b>Data analysis</b>	<b>14</b>
4.1	Data acquisition and processing . . . . .	14
4.2	Event reconstruction . . . . .	14
4.3	Event selection . . . . .	15
4.4	Analysis prerequisites . . . . .	15
4.4.1	Fiducial $\psi(nS) \rightarrow \mu^+\mu^-$ differential production cross section . . . . .	16
4.4.2	Non-prompt fraction . . . . .	16
4.4.3	Reconstruction and trigger efficiency . . . . .	16
4.4.4	Acceptance . . . . .	17
4.5	Fitting procedure . . . . .	18
<b>5</b>	<b>Results</b>	<b>21</b>

5.1	$J/\psi$ results . . . . .	21
5.2	$\psi(2S)$ results . . . . .	23
5.3	$\psi(2S)$ to $J/\psi$ production ratio . . . . .	24
<b>6</b>	<b>Summary</b>	<b>27</b>

# Chapter 1

## Introduction

The main goal of this research project is the comparison of measured  $J/\psi$  and  $\psi(2S)$  production cross section with results of the ATLAS collaboration at  $\sqrt{s} = 8$  TeV. The production cross section are measured for both prompt and non-prompt sources and restricted to the fiducial region only.

In addition the results need to be compared with previous measurement at  $\sqrt{s} = 7$  TeV to prove that fitting procedure and model used in the analysis is stable under multiple initial conditions.

The main improvement, with respect to my previous analysis, is implementing acceptance maps and inclusion of new trigger efficiency maps. This was necessary because another effects affecting the efficiency were observed during analysis. After the corrections to the kinematic acceptance, trigger efficiency and reconstruction efficiency the results should be comparable with official ATLAS analysis.

The fitting procedure was also improved to simply determine the prompt and non-prompt  $J/\psi$  and  $\psi(2S)$ . In addition the pseudo-proper time is fitted simultaneously with cross section and the fit uses unbinned data.

This analysis uses official trigger efficiency maps and reconstruction maps produced by the BPHYS work group of ATLAS collaboration, but this analysis is not connected to the official  $J/\psi$ ,  $\psi(2S)$  production cross section analysis.

# Chapter 2

## Theoretical background

### 2.1 Standard model

Particle physics is dealing with the particles that are the constituents of what is usually referred to as matter and radiation. There were many models trying to describe well known phenomena and physical laws. In the 1970s, the Standard Model (SM) of particles and their interactions was formed. This model is in best agreement with experimental data. The Standard Model assumes, that our world is made of 17 elementary particles. The first group is called fermions and has a half-integer spin. The second group is called bosons and has an integer spin. The particles interact via four known types of forces: electromagnetic, strong, weak and gravitational which latter not being part of the SM. The complete list of elementary particles and some of their properties is shown in Tab. 2.1.

#### 2.1.1 Fundamental interactions

Interactions in the Standard Model are realized as an exchange of mediating bosons, characteristic to the type of interaction between its constituents. Due to their character, they are frequently called exchange interactions.

*Electromagnetic* interaction is mediated by a massless photon and it has infinite range. This interaction acts between charged particles. The theory describing the electromagnetic interaction is called quantum electrodynamics (QED) and it later laid the ground of the quantum field theory (QFT), the framework for description of other interactions in the Standard Model.

*Strong* interaction binds quarks together in hadrons and is mediated by the exchange of massless gluons. Strong force is the strongest force compared to other forces, and its range is limited to 1 fm.

*Weak* interaction is responsible for the relatively slow processes of  $\beta$  decay. The mediators of this interaction are  $W^\pm$  and  $Z^0$  bosons. It is characterised by long lifetimes and small cross sections.

*Gravitational* interaction acts between all particles. Gravitational force is the weakest of all fundamental forces, and is almost  $10^{-38}$  times weaker than strong interaction. Due to this fact, gravitational interaction is neglected in the SM. In the some particle theories, this interaction is mediated by a hypothetical particle graviton with spin 2.

	Symbol	Name	Mass	Charge	Spin
Quarks	$u$	up	$2.3^{+0.7}_{-0.5}$ MeV	2/3	1/2
	$d$	down	$4.8^{+0.5}_{-0.3}$ MeV	-1/3	1/2
	$s$	strange	$95 \pm 5$ MeV	-1/3	1/2
	$c$	charm	$1.275 \pm 0.025$ GeV	2/3	1/2
	$b$	bottom	$4.18 \pm 0.03$ GeV	-1/3	1/2
	$t$	top	$173.07 \pm 0.52 \pm 0.72$ GeV	2/3	1/2
Leptons	$e$	electron	$0.510998928 \pm 0.000000011$ MeV	-1	1/2
	$\mu$	muon	$105.6583715 \pm 0.0000035$ MeV	-1	1/2
	$\tau$	tau	$1776.82 \pm 0.16$ MeV	-1	1/2
	$\nu_e$	e-neutrino	$< 2$ eV	0	1/2
	$\nu_\mu$	$\mu$ -neutrino	$< 0.19$ MeV	0	1/2
	$\nu_\tau$	$\tau$ -neutrino	$< 18.2$ MeV	0	1/2
Gauge bosons	$\gamma$	photon	0	0	1
	$W^{+-}$	W	$80.385 \pm 0.015$ GeV	$\pm 1$	1
	$Z$	Z	$91.1876 \pm 0.0021$ GeV	0	1
	$g$	gluon	0	0	1
	$H$	Higgs	$125.9 \pm 0.4$ GeV	0	0 [3]

Table 2.1: The list of particles in the Standard Model. [4]

### 2.1.2 Quarks

Quarks are structureless fermions with spin 1/2 and are structural elements of mesons and baryons. Six quarks are known at present, as can be seen in table 2.1. The quarks exist in three generations. Almost all matter around us is made of  $u$  and  $d$  quarks, which belong to the first generation. In the 1960s, new particles were observed which decay slower than was expected. To this particles was assigned an additional quantum number  $S$  called strangeness. After observation of  $c$ ,  $b$  and  $t$  quarks, additional quantum numbers (charm, beauty and top) were assigned to baryons which carry these quarks. The first three quarks are referred to as light quarks  $q$  and the other three quarks are referred to as heavy quarks  $Q$ .

### 2.1.3 Leptons

At present, six leptons are known, which are similarly to quarks categorized into three generations. There are three charged leptons and to each of them there is a neutral neutrino. The masses or mass limits of leptons are given in table 2.1.

Neutrinos are specific with masses small in comparison to the corresponding charged leptons. Although the neutrinos have mass, in the Standard Model they are assumed to be massless. The neutrinos are also unique in that only negative projection of total angular momentum onto  $z$  axis was observed. This corresponds to pure helicity <sup>1</sup> state  $H = -1$  (left-handed). The latest measure-

<sup>1</sup>Helicity is the projection of the spin  $\vec{S}$  onto the direction of momentum  $\vec{p}$ . [5]

ment of the Planck detector provides the upper limit for sum of the neutrino masses  $m_{\nu_i}$  [6]

$$\sum_i m_{\nu_i} < 0.25 \text{ eV}. \quad (2.1)$$

### 2.1.4 Antiparticles

To every particle exists corresponding antiparticle with same mass and lifetime but with opposite charge and magnetic moment.

The existence of antiparticles is a general property of both fermions and bosons. The first observed antiparticle was the antiparticle of an electron, which is called positron. Due to the conservation laws, fermions must be created and destroyed in pairs. This mechanism is called pair-production and annihilation.

## 2.2 Strong interaction

### 2.2.1 Colour

The colour is an additional internal degree of freedom of quarks. This degree of freedom was introduced after the observation of  $\Delta^{++}$  baryon which is made of three up quarks. This baryon will break the Pauli exclusion principle without introduction of another degree of freedom, called colour charge. Thus, there are three colors red, green and blue with their respective anticolours. As mentioned above, strong interaction is mediated by an exchange of massless gluons. These gluons carry colour and anticolour charge and provide colour interaction between two quarks. With three colours and three anticolours, there is a coloured gluon octet with possible combinations taking form of

$$r\bar{b}, r\bar{g}, b\bar{g}, b\bar{r}, g\bar{r}, g\bar{b}, \frac{1}{\sqrt{2}}(r\bar{r} - b\bar{b}), \frac{1}{\sqrt{6}}(r\bar{r} + b\bar{b} - 2g\bar{g}), \quad (2.2)$$

and a colourless gluon singlet  $\frac{1}{\sqrt{3}}(r\bar{r} + b\bar{b} + g\bar{g})$ .

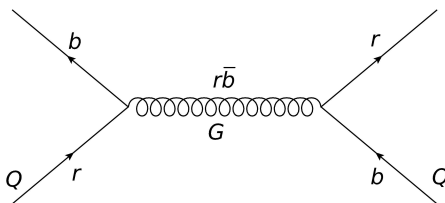


Figure 2.1:  $QQ'$  interaction via coloured gluon exchange. The time runs from bottom to top.

The colour charge of the strong interaction is analogous to the electric charge in electromagnetic interaction. Both forces are mediated by massless vector particles, but compared to photons, gluons can interact with each other. This phenomena is called gluon self coupling. Due to gluon self coupling, the colour charge exhibits a particular behavior called antiscreening. It is the opposite to the screening of electric charge in QED.

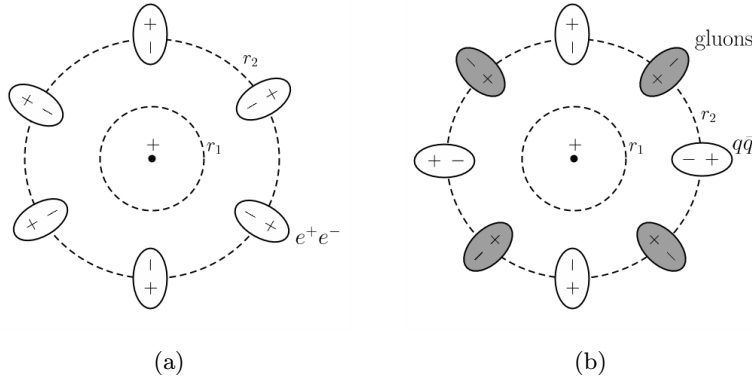


Figure 2.2: Screening of electric charge by virtual electron-positron pairs in (a) and antiscreening of the colour charge by gluons and screening by quarks in (b). [7]

Both baryons and mesons must be colourless, thus the quarks and gluons are confined inside hadrons. No free quarks were observed, with the exception of the top quark, which decays before it has a chance to hadronize.

### 2.2.2 QCD

The theory describing the interactions between quarks and gluons based on a colour exchange is called quantum chromodynamics (QCD). Despite photons and gluons being massless, the QCD potential takes a different form due to the differences between those forces. The simplest potential model for mesons that describes strong interaction is called Cornell potential model and it takes form

$$V_s(r) = -\frac{4}{3} \frac{\alpha_s}{r} + kr, \quad (2.3)$$

where  $\alpha_s$  is the strong interaction coupling and  $k$  is a free parameter. The first part of the equation is similar to the Coulomb potential with a factor of  $\frac{4}{3}$ . This factor arises from eight colour gluon states averaged over three quark colours. The factor is divided by 2 from the definition of  $\alpha_s$ . The second, linear term is associated with colour confinement at large  $r$ .

The Cornell potential can be extended by inclusion of the spin interaction between quarks. These spin-dependent potentials are assumed to be dominated by a one-gluon exchange and consist of spin-spin, tensor and spin-orbit terms. For a system of two quarks, the potential takes the following form [8]:

$$V_{q\bar{q}} = -\frac{4}{3} \frac{\alpha_s}{r} + \sigma r + \frac{32\pi\alpha_s}{9m_q^2} \delta(r) \mathbf{S}_q \cdot \mathbf{S}_{\bar{q}} + \frac{1}{m_q^2} \left[ \left( \frac{2\alpha_s}{r^3} - \frac{b}{2r} \right) \mathbf{L} \cdot \mathbf{S} + \frac{4\alpha_s}{r^3} \mathbf{T} \right], \quad (2.4)$$

where the  $\mathbf{L}$  is an orbital momentum,  $\mathbf{S}_q$  is a spin momentum of a particular quark,  $\mathbf{S} = \mathbf{S}_q + \mathbf{S}_{\bar{q}}$  and  $\mathbf{T}$  is a tensor term.

These extended models give better results, but still they are not satisfactory. Thus, the new interquark potential models are being developed and tested.

### 2.2.3 Running coupling

Charge screening in the QED (screening) and QCD (antiscreening) leads to the concept of a running coupling (the energy dependence of a strong coupling). In the QED, the coupling becomes large at (very) short distance and large energies, but its effect is small. In the QCD, the antiscreening effect causes the strong coupling to become small at short distance (large momentum transfer). This causes the quarks inside hadrons to behave more or less like free particles. This property of the strong interaction is called asymptotic freedom.

On the other hand, at the increasing distance, the coupling becomes so strong that it is impossible to isolate a quark from a hadron. In addition, if the quark pair receives more energy than is necessary for the production of a new quark antiquark pair, then it is energetically favourable to produce a new quark pair. This mechanism is called colour confinement.

Using perturbative QCD (pQCD) calculations and experimental data, the coupling constant of the QCD can be shown to have the following energy scale-dependence

$$\alpha_s(Q) = \frac{2\pi}{\beta_0 \ln \frac{Q}{\Lambda_{\text{QCD}}}}, \quad (2.5)$$

where  $\beta_0 = 11 - \frac{2}{3}n_f$ , with  $n_f$  being the number of the active quark flavor, and  $\Lambda_{\text{QCD}}$  is the QCD scale [4]. The value of  $\Lambda_{\text{QCD}} = (0.339 \pm 0.010)$  GeV is determined by experiments. This dependence is valid only for  $Q^2 \gg 2\Lambda^2$ , where the  $Q$  is transferred momentum. The summary of measurements of  $\alpha_s(Q)$  from multiple experiments is shown in Figure 2.3.

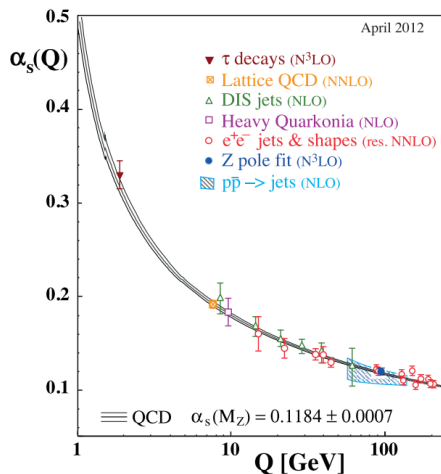


Figure 2.3: Summary of measurements of  $\alpha_s(Q)$  as a function of the respective energy scale  $Q$ . The respective degree of the QCD perturbation theory used in the extraction of  $\alpha_s$  is indicated in brackets (NLO: next-to-leading order; NNLO: next-to-next-to leading order; res. NNLO: NNLO matched with resummed next-to-leading logs; N<sup>3</sup>LO: next-to-NNLO)<sup>2</sup>. [4]

<sup>2</sup>NLO etc. are the levels of the perturbation QCD theory into which the Feynman diagrams are counted.



### 2.3.1 Color Singlet Model

In the Color Singlet Model (CSM), the perturbative and non-perturbative parts of the quarkonium production process are completely correlated. In this model the  $Q\bar{Q}$  pair is directly prepared with the proper quantum numbers in the initial hard subprocess, only then is non-zero probability to form the corresponding final state. The gluons can not adjust quantum numbers in this theory and they only serve to generate binding potential.

The CSM correctly predicts the normalization and momentum dependence of the  $J/\psi$  photoproduction rate, but it fails to adequately reproduce other available data on quarkonium production. Its predictions of the directly produced  $J/\psi$  and  $\psi(2S)$  hadroproduction rates are smaller by more than an order of magnitude.

### 2.3.2 Color Evaporation Model

In the Color Evaporation Model (CEM), the perturbative and non-perturbative parts of the quarkonium production process are considered to be uncorrelated. The production cross section of all quarkonia states in CEM is some fraction of the overall  $Q\bar{Q}$  pairs cross section below the  $H\bar{H}$  threshold where  $H$  is the lowest mass hadron with corresponding heavy quark. The CEM cross section is then simply the  $Q\bar{Q}$  production cross section with a cut on the pair mass. In the CEM there are not any constraints on the color or spin of the final state, because the produced  $Q\bar{Q}$  pair neutralizes its color by interaction with the collision-induced color field, thus the name "color evaporation". The interaction with color field can be described by the multiple soft gluon emissions. The soft interactions assumed to be universal and the effect on the dynamics of the quarkonium state is negligible.

The CEM predicts zero polarization of the  $J/\psi$  which is valid only for the low  $p_T$  regions.

### 2.3.3 Nonrelativistic QCD Factorization Model

The Nonrelativistic QCD Factorization Model based on the effective field theory Nonrelativistic QCD (NRQCD) and lies somewhere between the previous two models. It predicts non-zero probability for any quark pair to produce almost any quarkonium state but the probability depends on the initial quantum state.

The quarkonium production cross section, in the NRQCD factorization model, can be written as

$$\sigma(H) = \sum_n \frac{F_n(\Lambda)}{m_Q^{d_n-4}} \langle 0 | \mathcal{O}_n^H | 0 \rangle, \quad (2.6)$$

where  $H$  is the quarkonium state  $\Lambda$  is the ultraviolet cutoff of the effective theory, the  $F_n$  are short-distance coefficients, and the  $\mathcal{O}_n^H$  are four-fermion operators, whose mass dimensions are  $d_n$ .

The short-distance coefficients  $F_n(\Lambda)$  are essentially the process-dependent partonic cross sections to make a  $Q\bar{Q}$  pair. The  $Q\bar{Q}$  pair can be produced in a color-singlet state or in a color-octet state. The short-distance coefficients are determined by matching the square of the production amplitude in NRQCD to full QCD. Because the  $Q\bar{Q}$  production scale is of order  $m_Q$  or greater, this matching can be carried out in perturbation theory.

The Nonrelativistic QCD Factorization Model successfully reproduced various quarkonia data and fits well on the experiment, but there are areas where there are still some problems. Recently the proof of the factorisation in heavy quarkonium production in NRQCD Factorization Model was introduced at next-to-next-to-leading order (NNLO) in coupling constant by using diagrammatic method of QCD [10].

## 2.4 $k_t$ -factorization approach [1]

This method how to do the factorization is based on another way how to describe the structure function, when incident gluons have non-zero transverse momenta in small-x region. This non-zero transverse momenta is result of the diffusion of parton evolution.

The exact expression for  $k_t$  gluon distribution can be obtained as a solution of the evolution equation which, contrary to the parton model case, is nonlinear due to interactions between the partons in small x region.

The biggest advantage compared to the classical parton model is that the main part of the NLO and even NNLO corrections are effectively included in the  $k_t$ -factorization approach, due to the off-shell gluons.

## Chapter 3

# The ATLAS detector [2]

The ATLAS (A Toroidal LHC ApparatuS) detector is general-purpose detector designed to study p-p collisions at the LHC (Large Hadron Collider) located in the CERN laboratory near Geneva, Switzerland. The LHC is designed to provide proton beams with  $\sqrt{s} = 14$  TeV with a design luminosity  $10^{34} \text{ cm}^{-2} \text{ s}^{-1}$  and reaction rate of 40 MHz. However during first run period, the LHC was operating at lower energy of  $\sqrt{s} = 7$  TeV in 2011 and  $\sqrt{s} = 8$  TeV in 2012. The reaction of 20 MHz rate is also lower than designed one. The LHC also provides collisions of  $\text{Pb}^{208}$  ions with energy  $\sqrt{s} = 5.5$  TeV per nucleon pair, at designed luminosity of  $10^{27} \text{ cm}^{-2} \text{ s}^{-1}$ .

The ATLAS cover almost the full solid angle around the collision point and is symmetric in the forward-backward direction with respect to the interaction point. It can be divided into barrel section, end-caps and forward region. The subdetectors can be divided into three sections inner detector (ID), calorimetry systems and muon spectrometer (MS).

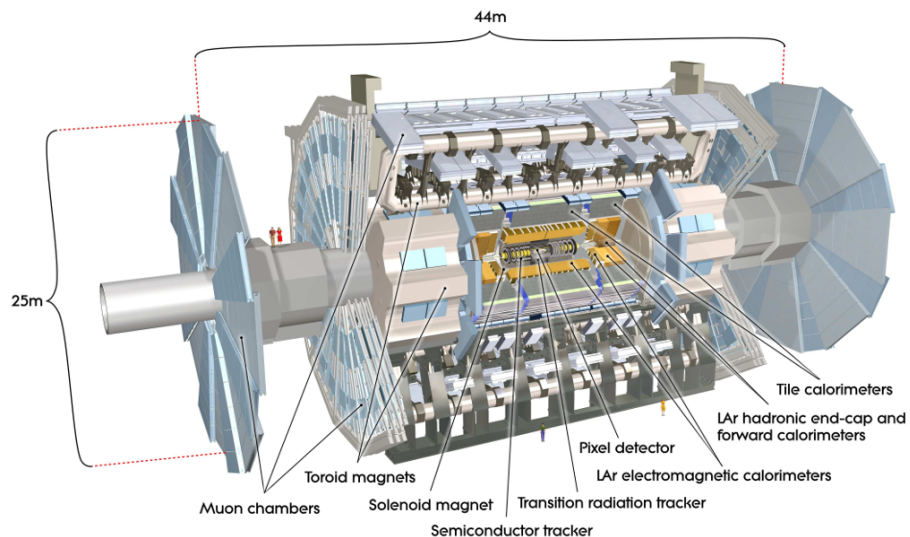


Figure 3.1: ATLAS detector cut-away view with its subdetectors highlighted. [2]

## 3.1 Inner detector

The inner detector is designed to provide an excellent momentum resolution for charged particles and both primary and secondary vertex position measurements with high precision in the pseudorapidity range of  $|\eta| < 2.5$ . The ID has to withstand high-radiation environment as the innermost subsystem of the ATLAS detector.

The ID is contained within a cylindrical envelope of a length of  $\pm 3512$  mm and of a radius of 1150 mm, and is immersed in a 2 T magnetic field generated by the central superconducting solenoid. The ID consists of a silicon pixel detector, a silicon strip detector (SCT) and a transition radiation tracker (TRT).

As can be seen in figure , the detectors are arranged as concentric cylinders around the beam axis in the barrel region. In the end-cap regions, there are pixel modules located on disks perpendicular to the beam axis. All detectors are mounted on a support structure, which is made of carbon fibers to ensure good mechanical properties, thermal conduction and low material budget.

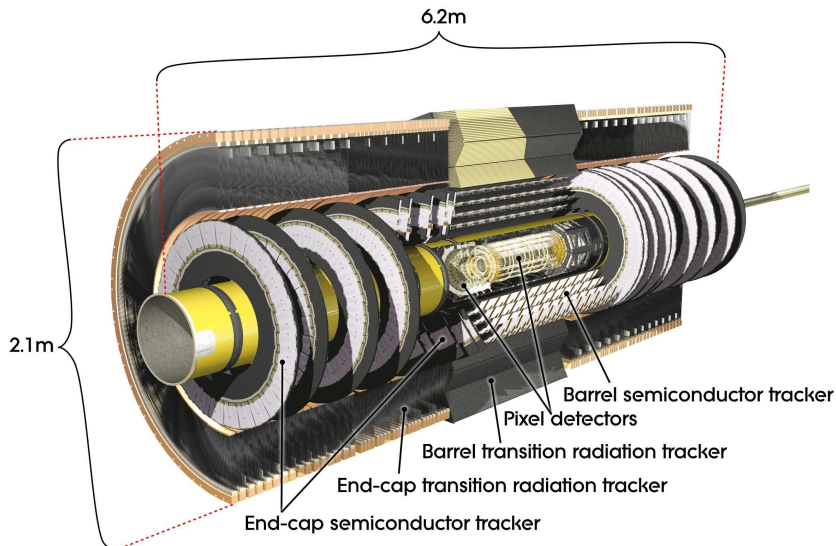


Figure 3.2: The schematic cut-away view of ATLAS inner detector. [2]

### 3.1.1 Pixel detector

The pixel detector contains three layers of the pixel modules in the barrel region (called ID layers 0–2) and two end-caps, each with three disk layers. The 0<sup>th</sup> layer is also referred to as B-layer. The layers are equipped by silicon pixel detectors with nominal pixel size of  $50 \times 400 \mu\text{m}^2$ . The sensor thickness is approximately  $250 \mu\text{m}$ . Silicon pixel sensors use planar technology with oxygenated n-type wafers and are read out on the  $n^+$ -implanted side of the sensor. The opposite side of the electrodes is in contact with a  $p^+$  layer. Each pixel sensor is bump-bonded through hole in the sensor passivation layer to front-end readout electronic chip. The pixel detector provides approximately 80.4 million readout channels in total.

During first long shutdown between years 2013 and 2015, upgrades are being made. The fourth layer of the pixel detector is added. This layer is placed between beampipe and current b-layer and is called the Insertable B-layer (IBL). This IBL is be equipped with new sensors using planar n-in-n and 3D double-sided n-in-p technology. These sensors have finer granularity of  $50 \times 250 \mu\text{m}^2$  and besides higher radiation tolerance, new readout chip FE-I4 has lower noise and power consumption.

### 3.1.2 SCT detector

SCT detector consist of four layers of double detectors in the barrel region (called ID layers 3–6) and two end-cap regions, each containing nine layers. Layers are equipped by modules which consist of  $80 \mu\text{m}$  pitch micro-strip sensors with thickness  $285 \pm 15 \mu\text{m}$ , providing  $R - \Phi$  coordinates.

Every two sensor modules are glued together in the barrel region within a hybrid module. On one detector layer, there are 2 sensor layers rotated within their hybrids by  $\pm 20 \text{ mrad}$  around the geometrical center of the sensor to measure both  $R - \Phi \times z$  coordinates.

For reason of cost and reliability, the sensors of SCT use classic single-sided p-in-n technology. The sensors are connected to a binary signal readout chips. In total, the SCT provides approximately 6.3 million readout channels.

### 3.1.3 Transition radiation tracker

Main purpose of TRT is to measure transition radiation of charged particles, in order to distinguish between light electrons and other particles, in the pseudo-rapidity range of  $|\eta| < 2.0$ . The TRT consist of 73 layers of straws in the barrel region and 160 straw planes in end-cap. Typically, the TRT gives 36 hits per track, but it provides only  $R - \Phi$  information.

The basic TRT detector elements are polyamide drift straw tubes with diameter of 4 mm filled by special gaseous mixture. The straw tube walls operates as cathodes, while the  $31 \mu\text{m}$  thick tungsten wire plated with  $0.5 \mu\text{m}$ – $0.7 \mu\text{m}$  layer of gold operates as anode. The total number of readout channels of TRT is approximately 351,000.

## 3.2 Calorimetry

Calorimetry system is designed to provide good energy resolution for measurement of electromagnetic and hadronic showers, and it must also limit punch-through into the muon system. Calorimetry system consist of two separate calorimeters using different designs suited to the widely varying requirements of the physics processes of interest, and it cover region up to  $|\eta| < 4.9$ . Over the  $\eta$  region matched to the inner detector, the fine granularity of the EM calorimeter is ideally suited for measurements of electrons and photons. There is coarser granularity in the rest of the detector, but calorimeters are precise enough to satisfy the physics requirements for jet reconstruction and  $E_T^{\text{miss}}$  measurement.

### 3.3 Muon spectrometer

The muon system is designed to detect charged particles exiting the barrel and end-cap calorimeters, and to measure muon momentum in the pseudorapidity range of  $|\eta| < 2.7$ . It measures properties of muon tracks bent by the large superconducting air-core toroid magnets. Detectors are situated in the barrel, end-cap and also in the transition regions ( $1.4 < |\eta| < 1.6$ ), where the tracks are bent by combination of barrel toroid and end-cap magnets. In the barrel region, tracks are measured in chambers arranged in three cylindrical layers around the beam axis, while in the transition and end-cap regions, the chambers are installed in planes perpendicular to the beam axis, also in three layers. Over most of the  $\eta$ -range, a precision measurement of the track coordinates is provided by the Monitored Drift Tubes (MDT). At large pseudorapidities, the Cathode Strip Chambers (CSC) with higher granularity are used to withstand demanding rate and background conditions.

The pseudorapidity range of  $|\eta| < 2.4$  is covered by an additional trigger system which is equipped with Resistive Plate Chambers (RPC) in the barrel ( $|\eta| < 1.05$ ) and Thin Gap Chambers (TGC) in end-cap ( $1.05 < |\eta| < 2.4$ ) regions, respectively. The main purpose is to provide fast track information for triggering purposes with well-defined  $p_T$  thresholds.

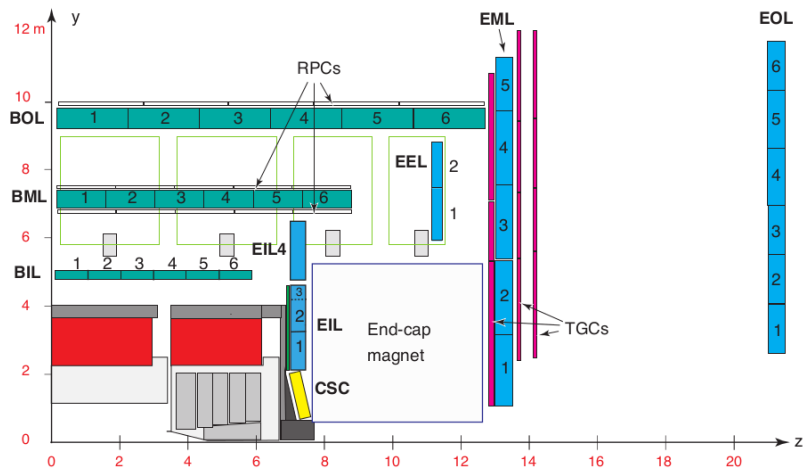


Figure 3.3: Cross-section of the quadrant of the muon system in a plane containing the beam axis. [2]

# Chapter 4

## Data analysis

### 4.1 Data acquisition and processing

The data were taken during LHC run1 in proton-proton collisions at both 7 TeV and 8 TeV where only the data collected with a stable beam operation are used. The criteria of quality were applied at the luminosity block levels, where the luminosity block, which lasts 60 seconds, is an atomic unit of the ATLAS data. To ensure the quality criteria the collected data are filtered by a Good Runs List (GRL), which take in account the prescale levels and triggers dead time. The integrated luminosity of both samples after trigger pass are  $2.2 \text{ fb}^{-1}$  for 2011 data and  $11.45 \text{ fb}^{-1}$  for 2012 data.

### 4.2 Event reconstruction

To measure the  $J/\psi$  and  $\psi'$  production cross section the di-muon channel was chosen, because the muons have clean detector signature. To reconstruct muon tracks, several different strategies have been developed using physics signatures in the inner detector, calorimeters and muon detector system. Muons can be classified into four categories according to the signatures left in the detector:

- *Standalone* muons are identified using only Muon Spectrometer. The tracks are extrapolated to the beam region to give the track parameters. Due to the position and momentum resolution of the muon chambers, their parameters are not measured as precisely as in other muon reconstruction types, but provide muons from higher pseudorapidity  $|\eta| < 2.7$ .
- *Combined* muons are formed by matching the Inner Detector track to the Muon Spectrometer track. Two algorithms, Staco and Muid, are used to identify the combined muons. They have the most precisely measured parameters.
- *Tagged* muons are the ID tracks matched to the hits in the muon segments in the Muon Spectrometer. There are two tagging algorithms, MuTag and MuGirl, propagating all inner detector tracks with a sufficient momentum out to the first station of the muon spectrometer and search for nearby segments.

- *Calorimeter* tagged muons use information about energy deposit in the calorimetry system matched to the ID tracks. The calorimeter muons have lower purity and efficiency than the muons reconstructed in the muon system.

To reconstruct di-muon candidates only combined muons are used to guarantee the purity of the signal. In 2011, two algorithms called the STACO (Statistical combination of the inner and outer track vectors) and Muid (a partial refit using the original hits in both ID and MS) are used to reconstruct dimuon candidates. Each of these algorithm produces its own chain called STACO and Muid. The STACO chain is used in this analysis for 2011 data, but the result should not be affected by this choice. Because both of these chains demonstrated their excellent capabilities of supporting physics analyses with muons, in 2012 they have been merged into a third, unified chain called Muons.

### 4.3 Event selection

The  $J/\psi$  and  $\psi(2S)$  candidates triggered by the trigger, which required two oppositely charged muons with  $p_T > 4$  GeV, have to pass multiple selection criteria. At first reconstructed candidate must fit within  $|\eta| < 2.3$  and invariant mass window of 2.6 GeV–4.0 GeV. Both offline reconstructed muons are restricted to  $p_T > 4$  GeV and  $|\eta| < 2.5$ . To ensure high purity of the signal each track is required to have at least one Pixel hit, five SCT hits and in case the track is within  $0.1 < |\eta| < 1.9$  at least six TRT hits. The maximum of the missing hits in the Pixel and SCT layers is 2. For TRT hits is additional condition to have at least 90% of hits over outliners. The muon candidates must to be matched within a cone  $\Delta R = \sqrt{(\Delta\eta)^2 + (\Delta\Phi)^2} < 0.01$  between each reconstructed muon candidate and the trigger identified candidates. This last constraint reject about 5% of candidates but ensures, that the trigger was fired by a measured muon and so the trigger unfolding can be performed.

### 4.4 Analysis prerequisites

The measurement is performed in several intervals of dimuon transverse momentum and absolute value of rapidity. The dimuon  $p_T$  range is restricted by kinematics conditions of  $p_T(\mu\mu) > 8$  GeV. The condition of sufficient statistics sets upper limit to  $p_T < 100$  GeV.

The measurement differs two compounds of signal prompt and non-prompt, for both  $J/\psi$  or  $\psi(2S)$  (hereafter called  $\psi(nS)$ ). The definition of prompt refers to the  $\psi(nS)$  states produced from short-lived QCD sources, this includes directly produced  $\psi(nS)$  in pp collision or indirectly produced  $\psi(nS)$  from feed-down from other charmonium states. If the decay chain includes long-lived particles such as b-hadrons then the  $\psi(nS)$  is labeled as non-prompt.

#### 4.4.1 Fiducial $\psi(nS) \rightarrow \mu^+\mu^-$ differential production cross section

Differential dimuon cross section in each bin for both prompt and non-prompt  $\psi(nS)$  is referred as

$$\frac{d^2\sigma(pp \rightarrow X \rightarrow \psi(nS))}{dp_T dy} Br(\psi(nS) \rightarrow \mu^+\mu^-) = \frac{N_{corr}^{p,np}}{\Delta p_T \Delta y \cdot \mathcal{L}}, \quad (4.1)$$

where  $\Delta p_T$  and  $\Delta y$  are bin widths,  $\mathcal{L}$  is the integrated luminosity of the data sample and  $N_{corr}^{p,np}$  is the number of dimuon signals for each  $p_T - y$  bin after background subtraction and corrected for detector inefficiencies for both prompt and non-prompt contributions. To determine the true number of  $J/\psi$  or  $\psi(2S)$  each recorded event is weighted by a weight  $w$ . The weight  $w$  is defined as

$$w^{-1} = \mathcal{A} \cdot \mathcal{E}_{reco} \cdot \mathcal{E}_{trig} \cdot \frac{1}{p}, \quad (4.2)$$

where  $\mathcal{E}_{reco}$  is the muon offline reconstruction efficiency,  $\mathcal{E}_{trig}$  is the trigger efficiency,  $p$  is the trigger prescale and  $\mathcal{A}$  is the kinematic acceptance.

#### 4.4.2 Non-prompt fraction

The pseudo-proper lifetime  $\tau$  is used as discrimination variable to measurement of the non-prompt fraction of  $\psi(nS)$  candidates. The pseudo-proper time is defined as lifetime in transverse plane described by following equation

$$\tau = \frac{L_{xy} \cdot m^{\psi(nS)}}{p_T^{\psi(nS)}}, \quad (4.3)$$

where  $L_{xy}$  is distance of  $\psi(nS)$  vertex from primary vertex measured in transverse plane, the  $m^{\psi(nS)}$  and  $p_T^{\psi(nS)}$  are invariant mass resp. transverse momentum of the candidate.

The non-prompt fraction is defined as number of non-prompt dimuons relative to the inclusively produced dimuons:

$$f_B = \frac{pp \rightarrow b + X \rightarrow \psi + X'}{pp \xrightarrow{\text{Inclusive}} \psi + X''}. \quad (4.4)$$

#### 4.4.3 Reconstruction and trigger efficiency

The reconstruction efficiency  $\mathcal{E}_{reco}$  for a given  $\psi(nS)$  candidate is calculated from single muon reconstruction efficiencies  $\mathcal{E}_\mu^\pm(p_T^\pm, \eta^\pm)$  as follows:

$$\mathcal{E}_{reco} = \mathcal{E}_\mu^+(p_T^+, \eta^+) \cdot \mathcal{E}_\mu^-(p_T^-, \eta^-). \quad (4.5)$$

The technique used for computation of correction is the same for both 2011 and 2012 measurements, but the maps final slightly differs. The offline single muon reconstruction efficiencies are determined from tag-and-probe study in dimuon decays and are function of  $p_T(\mu)$  and  $q \times \eta(\mu)$ , where  $q$  is a charge of the muon.

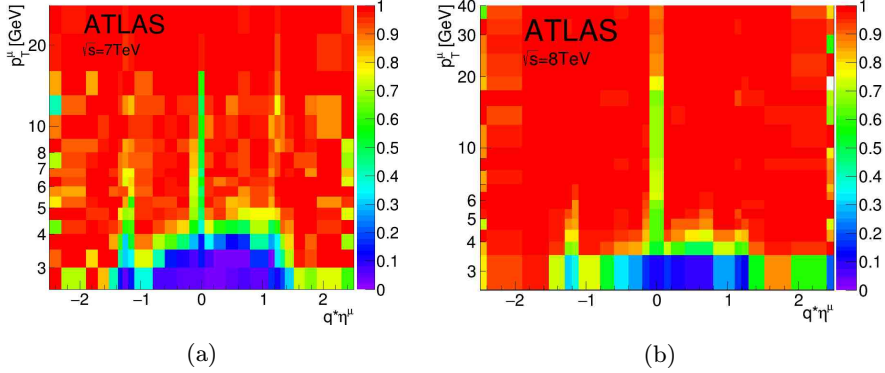


Figure 4.1: The reconstruction efficiency maps for both 7 TeV and 8 TeV data as a function of the muon charge-signed pseudorapidity and muon  $p_T$ .

Similar to reconstruction efficiency, the trigger efficiency  $\mathcal{E}_{trig}$  for given  $\psi(nS)$  are calculated from single muon efficiencies  $\mathcal{E}_{RoI}^{\pm}(p_T^{\pm}, q, \eta^{\pm})$ . The additional correction factor  $c_{\mu\mu}(\Delta R, |y^{\mu\mu}|)$  must be used to include dimuon effects such as overlapping RoIs or vertex quality. The trigger efficiency is then computed as

$$\mathcal{E}_{trig} = \mathcal{E}_{RoI}^{+}(p_T^{+}, q, \eta^{+}) \cdot \mathcal{E}_{RoI}^{-}(p_T^{-}, q, \eta^{-}) \cdot c_{\mu\mu}(\Delta R, |y^{\mu\mu}|). \quad (4.6)$$

This correction factor, computed from tag-and-probe, is divided in three bins of rapidity. Because the efficiency maps calculated directly from 2012 data have issue with low  $p_T$  and high rapidity events additional MC correction ave to be applied. This is made by fraction of two additional maps for low  $p_T$  tag muons, which are not available from data, and high  $p_T$  EF\_mu18 trigger as well from MC simulation. The efficiencies were provided by the ATLAS B-physics group and are preliminary.

In 2012 data were observed an issue, where the 4% of events which fired the "EF\_2mu4T\_Jpsimumu\_L2StarB" trigger have not stored its trigger objects. Unfortunately, these events are correlated and thus should not be omitted from the analysis. To handle this out additional systematics should be applied.

#### 4.4.4 Acceptance

The kinematic acceptance  $\mathcal{A}(p_T, y)$  is the probability that the muons from  $\psi(nS)$  with rapidity  $y$  and transverse momentum  $p_T$  fall into fiducial volume of the ATLAS detector. The acceptance maps are computed using Monte Carlo generator applying selection criteria on particle momenta and rapidity to emulate the detector geometry.

The acceptance also depend on spin alignment of  $\psi(nS)$  production mechanism, which is not well known for LHC conditions. This affects angular distribution of dimuon decays. The general decay frame of  $\psi(nS)$  candidate is given by

$$\frac{d^2 N}{d \cos \theta^* d \phi^*} \propto 1 + \lambda_{\theta} \cos^2 \theta^* + \lambda_{\phi} \sin^2 \theta^* \cos 2\phi^* + \lambda_{\theta\phi} \sin 2\theta^* \cos \phi^*, \quad (4.7)$$

where the  $\theta^*$  is the angle between the direction of the positive muon momentum in the  $\psi(nS)$  decay frame and the  $\psi(nS)$  line of flight. The  $\phi^*$  is the angle between the  $\psi(nS)$  production and decay planes in the lab frame. The  $\lambda_\theta$ ,  $\lambda_\phi$  and  $\lambda_{\phi\theta}$  are related to the spin density matrix elements of the dimuon spin wave function.

The different production scenarios were studied such as longitudinal polarization where  $\lambda_\theta = -1$ ,  $\lambda_\phi = \lambda_{\phi\theta} = 0$  or transverse alignment where  $\lambda_\theta = +1$ ,  $\lambda_\phi = \lambda_{\phi\theta} = 0$  etc., but as the main polarization scenario is used isotropic distribution independent on  $\theta^*$  and  $\phi^*$  with  $\lambda_\theta = \lambda_\phi = \lambda_{\phi\theta} = 0$ .

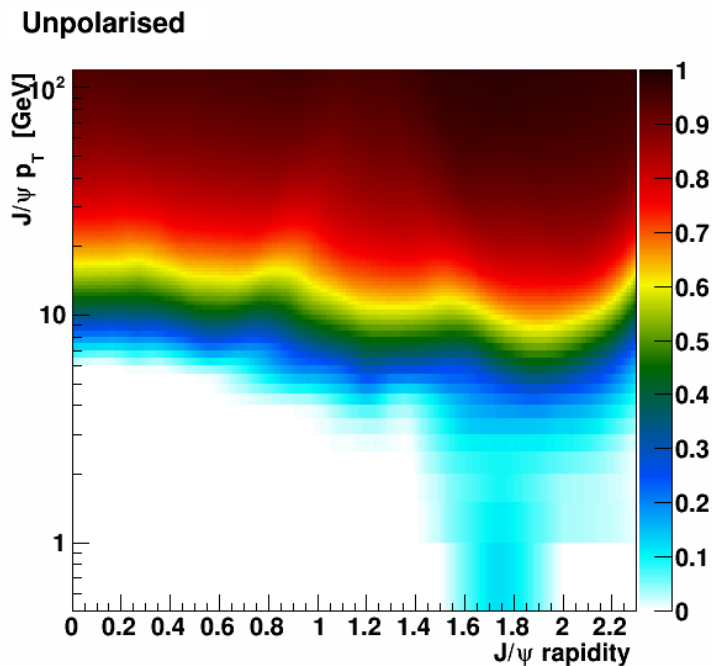


Figure 4.2: The acceptance map of unpolarized  $J/\Psi$  hypothesis, produced as a function of the  $p_T$  and rapidity.

## 4.5 Fitting procedure

In each bin of  $p_T$  and  $|y|$  was made two-dimensional unbinned maximum likelihood fit of weighted events. The each bin was fitted separately with own sets of parameters. The fit consist of prompt and non-prompt contributions for both  $J/\psi$  and  $\psi(2S)$  and three sets of background one for prompt contributions and two for non-prompt background includes flipped decay with negative decay times related with miss-reconstructed or non-coherent dimuon pairs.

The final likelihood function takes following form:

$$\mathcal{L} = \sum_{i=1}^7 f_i \cdot P_i(m, \tau) \otimes R(\tau), \quad (4.8)$$

Source	Type	invariant mass frame	pseudo-proper time frame
$J/\psi$	prompt	$CB(\sigma_{1p}, \mu_1, \alpha_1, n)$	$\delta(0)$
	non-prompt	$CB(\sigma_{1n}, \mu_1, \alpha_1, n)$	$E_1(\tau_1)$
$\psi(2S)$	prompt	$G(\sigma_{2p}, \mu_2)$	$\delta(0)$
	non-prompt	$G(\sigma_{2n}, \mu_2)$	$E_2(\tau_2)$
Background	prompt	$L(a_1)$	$\delta(0)$
	non-prompt	$E_3(\lambda_1)$	$E_4(\tau_3)$
	non-prompt	$E_5(\lambda_2)$	$E_6(-\tau_4)$

Table 4.1: Components of overall fit function, where CB means Crystal Ball distribution, G is gaussian distribution, E exponential,  $\delta$  is dirac delta function and L is linear function.

where  $f_i$  is the normalization factor,  $P_i(m, \tau)$  is two-dimensional probability function for all contributions and  $R(\tau)$  is the resolution term common for all pseudo-proper lifetime distributions.

For the description of the both prompt and non-prompt signal in invariant mass frame the CrystallBall distribution was used. In the pseudo-proper time frame is used the dirac function convolved with the resolution function for prompt and one-sided exponential convolved with the same resolution function for non-prompt. The resolution function is described with the gaussian distribution and is the same for all of the pseudo-proper time distributions.

The background is composed of three components. The prompt component of background is described by the linear function in invariant mass frame and dirac function convolved with the resolution function in pseudo-proper time frame. The non-prompt components of the background are two. The first one is exponential for invariant mass frame and single sided exponential convolved with the resolution function in pseudo-proper time frame. The second one is exponential for invariant mass frame and flipped single sided exponential convolved with the resolution function in pseudo-proper time frame. The negative part of the background is connected with miss match during reconstruction and combinatoric background. All of the components that contributes to the overall fit function are concluded in following table 4.1.

From the fit result can be extracted many useful dependencies such as  $\psi(2S)$  to  $J/\psi$  production ratio,  $J/\psi$  and  $\psi(2S)$  production cross section and non-prompt to prompt fraction for both  $J/\psi$  and  $\psi(2S)$ .

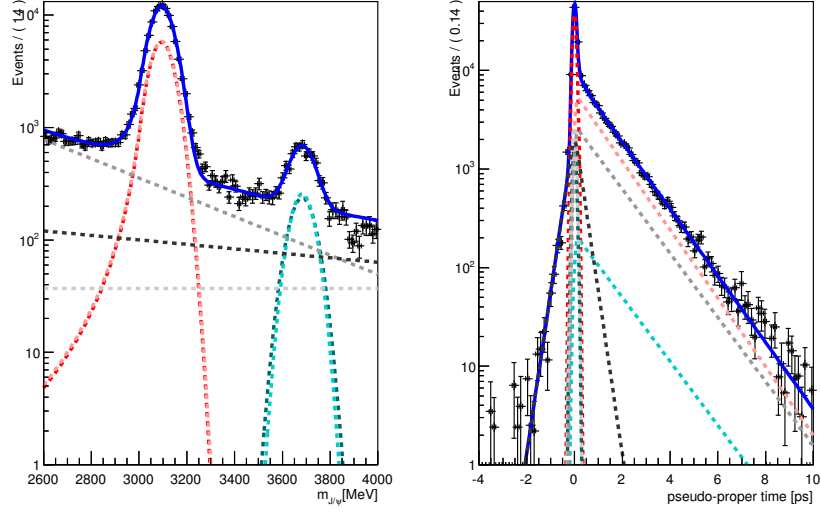


Figure 4.3: The projection of simultaneous fit result for  $18 \text{ GeV} < p_T < 20 \text{ GeV}$  and  $0.75 < |y| < 1.00$  bin in 7 TeV data. The invariant mass projection is presented on the left side and the pseudo-proper time projection on the right side.

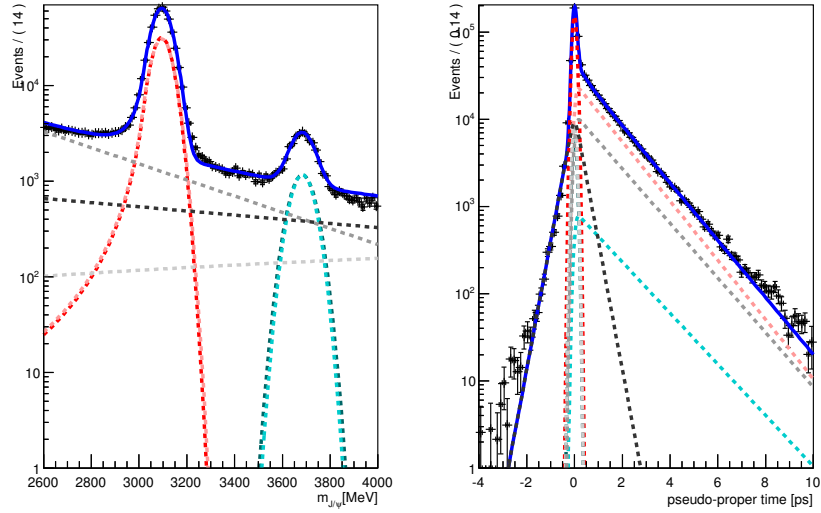


Figure 4.4: The projection of simultaneous fit result for  $18 \text{ GeV} < p_T < 20 \text{ GeV}$  and  $0.75 < |y| < 1.00$  bin in 8 TeV data. The invariant mass projection is presented on the left side and the pseudo-proper time projection on the right side.

# Chapter 5

## Results

The following chapter summarize all results obtained from the simultaneous unbinned maximum likelihood fits. The results are presented with statistical uncertainties only. The systematic uncertainties are not calculated yet, but the most significant uncertainties would be originated from the polarization model, trigger and reconstruction efficiencies, fit model and luminosity.

### 5.1 $J/\psi$ results

As can be seen in the figures 5.1 and 5.2, the  $J/\psi$  fit results are stable for both 7 TeV and 8 TeV data. Even in the last rapidity bin  $2.00 < |y| < 2.30$ , where the statistical sample is smaller, the results is continuous without any bumps. Only few bins shows irregular behavior, but this is mainly because of unsuccessful background fit.

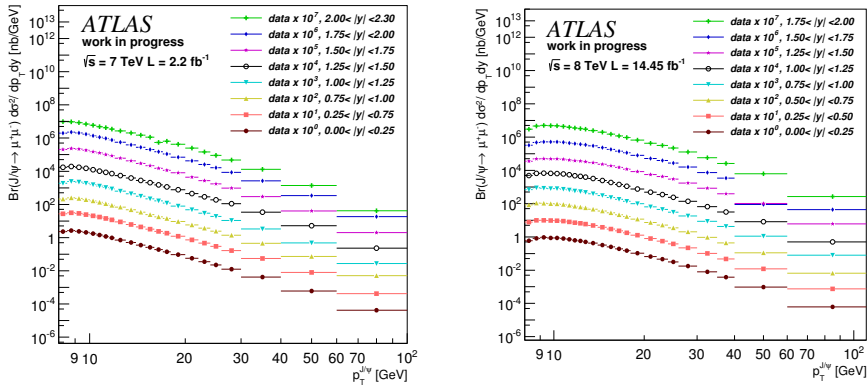


Figure 5.1: The  $J/\psi$  differential production cross section for 7 TeV data on the left and 8 TeV data on the right in several bins in rapidity.

As can be seen in figure 5.3 the prompt and non-prompt contribution to the total cross section can be easily calculated, because they are direct results of

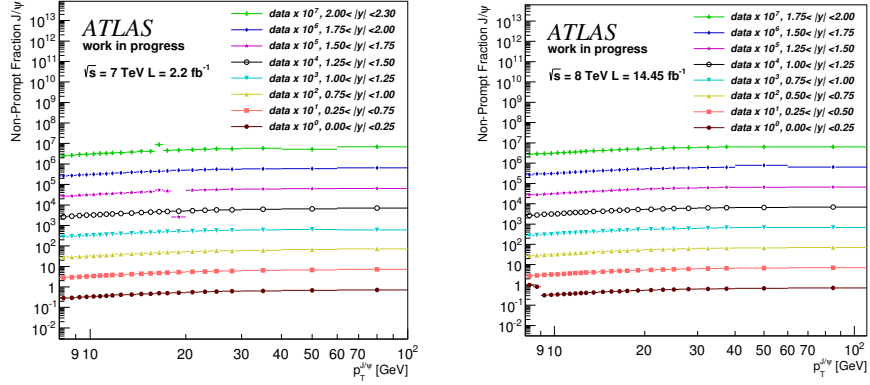


Figure 5.2: The non-prompt  $J/\psi$  production fraction for 7 TeV data on the left and 8 TeV data on the right in several bins in rapidity.

the fit. This can be done for  $\psi(2S)$  as well as  $J/\psi$ .

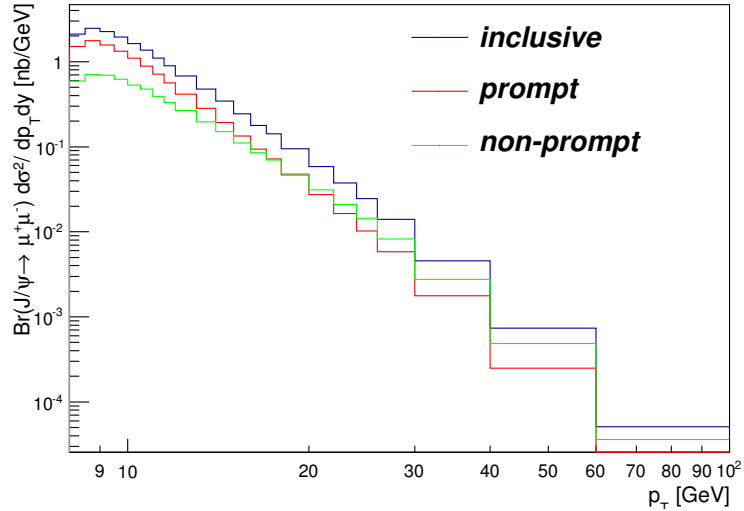


Figure 5.3: The prompt and non-prompt contributions to the total cross section in  $0.75 < |y| < 1.00$  rapidity bin.

The figure 5.4 shows comparison of my measurement with official ATLAS analysis [11], where the my results shows some systematics shift. My measured cross section are larger in the high  $p_T$  but in the low  $p_T$  are there is a rapid decrease. On the other hand the non-prompt fraction of  $J/\psi$  is in agreement with official ATLAS analysis without any irregularities. The reason of this disagreement are not yet known.

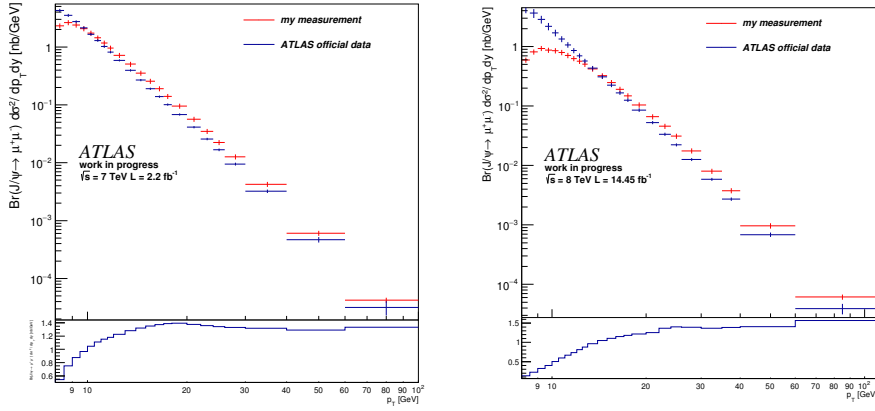


Figure 5.4: The official ATLAS  $J/\psi$  cross section measurement compared with my results. The result for 7 TeV is on the left side for 8 TeV is on the right side.

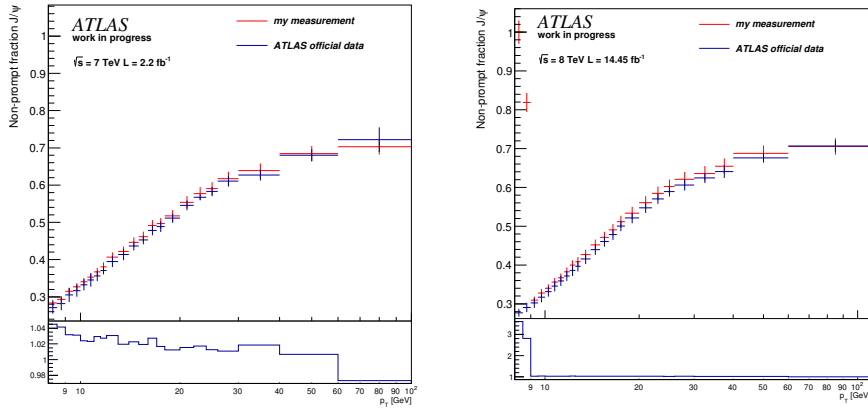


Figure 5.5: The official ATLAS  $J/\psi$  non prompt fraction measurement compared with my results. The result for 7 TeV is on the left side for 8 TeV is on the right side.

## 5.2 $\psi(2S)$ results

The  $\psi(2S)$  fit results are less stable especially in the last bin of rapidity and in the bins with  $p_T > 60$  GeV. In these bin the statistics for  $\psi(2S)$  is insufficient and the fit model have problems.

The reduction of number of free parameters may solve the problem with stability, but on the other hand reduce the flexibility of the fit.

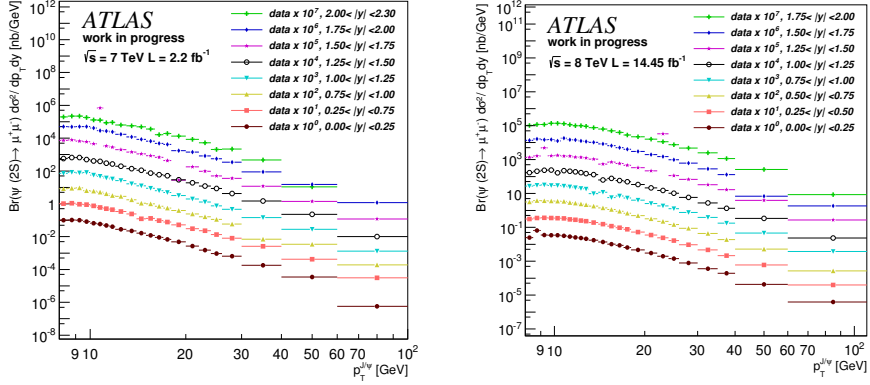


Figure 5.6: The  $\psi(2S)$  differential production cross section for 7 TeV data on the left and 8 TeV data on the right in several bins in rapidity.

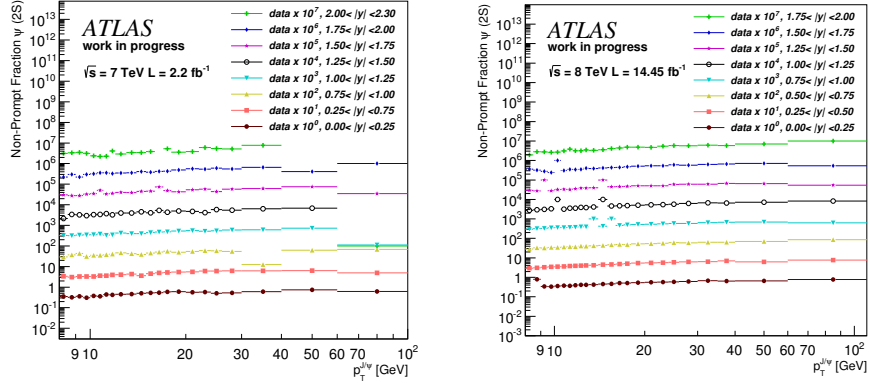


Figure 5.7: The non-prompt  $\psi(2S)$  production fraction for 7 TeV data on the left and 8 TeV data on the right in several bins in rapidity.

### 5.3 $\psi(2S)$ to $J/\psi$ production ratio

The production  $\psi(2S)$  to  $J/\psi$  ratio seems to be constant with no dependence on rapidity or  $p_T$ . The instability of  $\psi(2S)$  contribution affect also this result, but many of the effects cancel each other, thus the result seems correct even in the bins with lack of data.

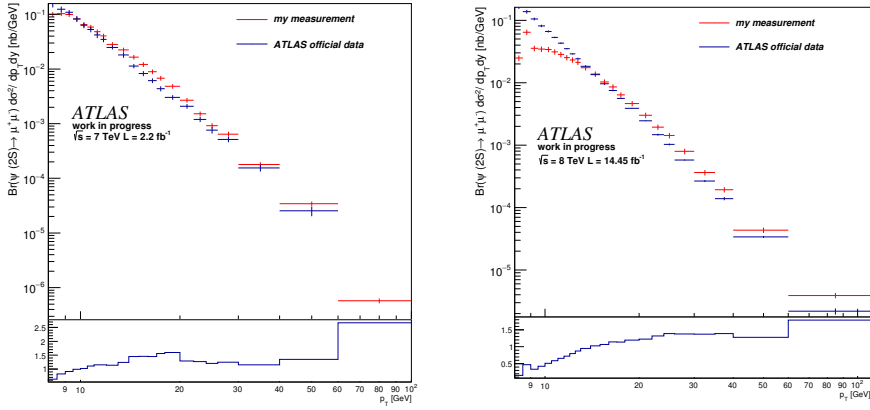


Figure 5.8: The official ATLAS  $\psi(2S)$  cross section measurement compared with my results. The result for 7 TeV is on the left side for 8 TeV is on the right side.

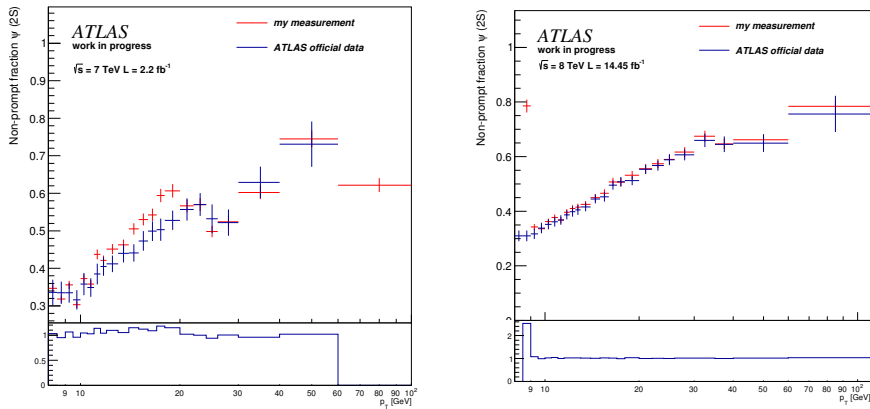


Figure 5.9: The official ATLAS  $\psi(2S)$  non prompt fraction measurement compared with my results. The result for 7 TeV is on the left side for 8 TeV is on the right side.

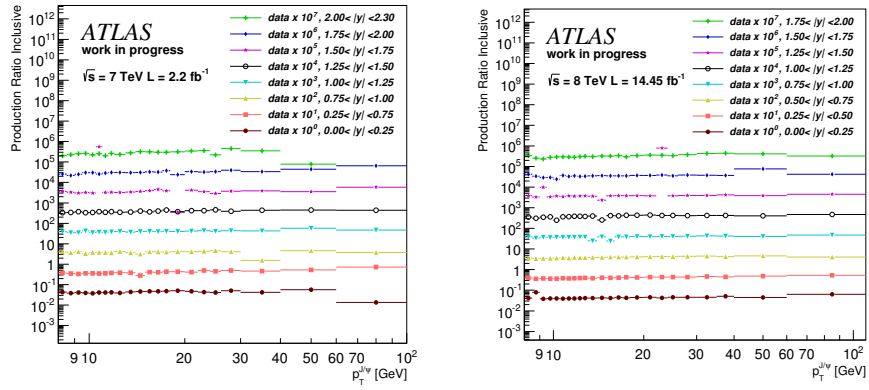


Figure 5.10: The  $\psi(2S)$  to  $J/\psi$  ratio for 7 TeV data on the left and 8 TeV data on the right in several bins in rapidity.

# Chapter 6

## Summary

This research project was devoted to a study of quarkonia states, particularly the  $J/\psi$  resonance and its first excited state  $\psi(2S)$ . The primary objective was the measurement of the inclusive production cross section of  $J/\psi$  and  $\psi(2S)$  at 8 TeV ( $14.45 \text{ fb}^{-1}$ ) with simple way to separate the prompt and non-prompt contribution. In addition the 7 TeV measurement ( $2.2 \text{ fb}^{-1}$ ) was made to prove the stability of the fitting procedure. For the purpose of this analysis the  $pp$  collision data recorded by the ATLAS experiment at the LHC were used.

The measured results are with agreement with previous measurement, but the stability of the fitting procedure must be improved. In both, 7 TeV and 8 TeV measurements, the significant systematics shift can be seen. The reason of this shift is not known yet, but most likely it is connected with implementation of trigger efficiencies or kinematic acceptance.

The fitting procedure is versatile, but the number of free parameters is too high. The way how to reduce number of free parameters is to fix some not so important parameters and the variation of its value include to the systematic uncertainty.

The further work on this analysis will be calculation of the systematics uncertainties and improvement of the fitting procedure because it became clear that the current model is not perfect.

This analysis is not connected to the official ATLAS  $J/\psi$ ,  $\psi(2S)$  production cross section analysis and serve only as the research work on this topic.

# Bibliography

- [1] M. G. Ryskin, Yu. M. Shabelski, and A. G. Shuvaev. Heavy quark production in hadron collisions. In *34th Annual Winter School on Nuclear and Particle Physics (PNPI 2000) Gatchina, Russia, February 14-20, 2000*, 2000.
- [2] The ATLAS Collaboration et al. . The atlas experiment at the cern large hadron collider. *Journal of Instrumentation*, 3(08):S08003, 2008.
- [3] Evidence for the spin-0 nature of the higgs boson using {ATLAS} data. *Physics Letters B*, 726(1-3):120 – 144, 2013.
- [4] J. Beringer et al. (Particle Data Group), Phys. Rev. D86, 010001 (2012) and 2013 partial update for the 2014 edition.
- [5] Donald H. Perkins. *Introduction to high energy physics*, volume 2. Addison-Wesley Reading, Massachusetts, 1987.
- [6] Elena Giusarma, Roland de Putter, Shirley Ho, and Olga Mena. Constraints on neutrino masses from Planck and Galaxy Clustering data. *Phys.Rev.*, D88(6):063515, 2013.
- [7] Felix Siebenhühner. Determination of the qcd coupling constant from charmonium. <http://theorie.ikp.physik.tu-darmstadt.de/nhc/pages/lectures/rhiseminar07-08/siebenhuehner.pdf>. Accessed: 2014-05-21.
- [8] Taichi Kawanai and Shoichi Sasaki. Heavy quarkonium potential from Bethe-Salpeter wave function on the lattice. *Phys.Rev.*, D89:054507, 2014.
- [9] Geoffrey T. Bodwin, Eric Braaten, and Jungil Lee. Comparison of the color-evaporation model and the NRQCD factorization approach in charmonium production. *Phys. Rev.*, D72:014004, 2005.
- [10] Gouranga C. Nayak. Proof of NRQCD Factorization at All Order in Coupling Constant in Heavy Quarkonium Production. 2015.
- [11] Measurement of the differential cross-sections of prompt and non-prompt production of  $J/\psi$  and  $\psi(2S)$  in  $pp$  collisions at  $\sqrt{s} = 7$  and 8 TeV with the ATLAS detector. Technical Report ATLAS-CONF-2015-024, CERN, Geneva, Jul 2015.